ACS OMEGA

http://pubs.acs.org/journal/acsodf

Article

Schottky Contacts to ZnO-Nanocoated SnSe Powders by Atomic Layer Deposition

Hogyoung Kim,* Myeong Jun Jung, Jongmin Byun, Min Hwan Lee, and Byung Joon Choi*

Cite This: *ACS Omega* 2022, 7, 41606−41613

Read Online

ACCESS | Metrics & More | Article Recommendations

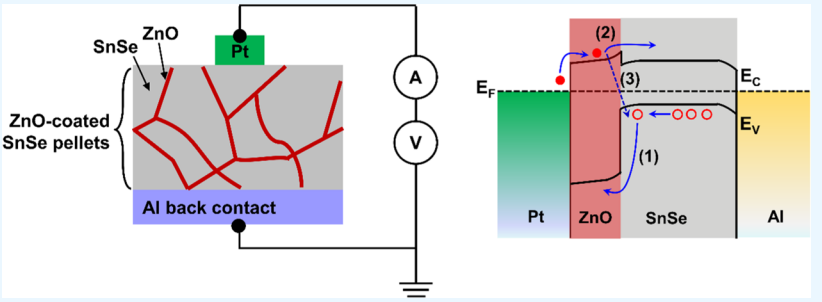

ABSTRACT: In this study, SnSe powders are nanocoated with ZnO grown by atomic layer deposition (ALD) with different ALD ZnO pulse cycles. Subsequently, the current transport mechanisms of Pt/ZnO-coated SnSe junctions are electrically investigated. A decrease in the current and an increase in the series resistance are observed at 300 K with increasing ZnO pulse cycles (*i.e.*, increasing the thickness of the ZnO layer). The series resistance is similar at 450 K for all samples. The difference in the barrier height for each sample is insignificant, thus indicating that the ZnO coating marginally alters the barrier height at the Pt/SnSe junction. The inhomogeneous Schottky barrier can explain both the forward and reverse bias current conduction. The lowest ideality factor observed for the SnSe sample with ZnO 100 cycles is related to the lowest standard deviation (*i.e.*, the lowest spatial fluctuation of the barrier height). Furthermore, the electrical conductivity is comparable to that of the sample without ZnO coating, thus suggesting that ZnO-coated SnSe by ALD can be considered to improve the thermoelectric device performance.

INTRODUCTION

Among selenium (Se)-based compound semiconductors, tin selenide (SnSe) (a band gap of approximately 1.0 eV) is a promising material because of its applications in thermoelectric devices,[1] photovoltaic cells,[2] field effect transistors (FETs),[3] and resistive memory devices.[4] SnSe is a layered semiconductor crystallized in an orthorhombic structure,[5] which prefers a Se-rich structure at low temperatures (below 600 K) and a Se-deficient composition at high temperatures (above 600 K).[6] Previous studies have suggested that the p-type conduction behavior of SnSe mainly originates from Sn vacancies (V_{Sn}), and other highly localized vacancies merely act as immobile carriers that do not participate in the current transport.[7]

In particular, the SnSe single crystal reportedly reached an outstanding figure of merit (ZT) of approximately 2.6 at 923 K owing to the ultralow thermal conductivity along the *b*-axis.[8] Here, the dimensionless ZT is expressed as $ZT = S^2\sigma T/\kappa$, where S, σ, T, and κ are the Seebeck coefficient, electrical conductivity, absolute temperature, and thermal conductivity, respectively. However, the poor mechanical properties, high cost, and slow process of single crystal growth for industrial applications have contributed to the increasing research on polycrystalline SnSe.[1] Compared with the SnSe single crystal, polycrystalline SnSe has a lower ZT (normally less than 1) because of the inferior power factor ($S^2\sigma$) resulting from grain boundaries, defects, and the random orientation of the constituent crystals.[9] Moreover, these factors can lead to a decreased thermal conductivity caused by the increased phonon scattering rate.[10] High doping has been reported to be less effective for polycrystalline SnSe because of less texturing, and it easily formed defects, thereby degrading the electrical properties.[11] Achieving an ultralow κ in polycrystalline SnSe comparable to the value of the SnSe single crystal has been the main strategy to enhance the thermoelectric performance.

Fine powder-based polycrystalline SnSe can enhance the phonon scattering with increased grain boundaries, which can decrease the thermal conductivity. Previous studies have

Received: August 30, 2022
Accepted: October 25, 2022
Published: November 3, 2022

https://doi.org/10.1021/acsomega.2c05584
ACS Omega 2022, 7, 41606−41613

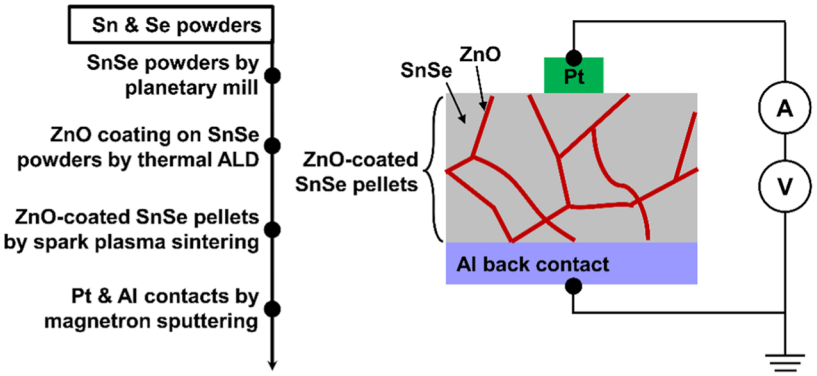

Figure 1. Schematic diagram of the prepared Pt/ZnO-coated SnSe devices.

Table 1. Carrier Concentration (p), Mobility (μ_H), Electrical Conductivity (σ), and Resistivity (ρ) Obtained From the Hall Effect Measurements at Room Temperature[a]

samples	p (cm^{-3})	μ_H ($cm^2\ V^{-1}\ s^{-1}$)	σ ($S\ cm^{-1}$)	ρ (Ωcm)
SnSe	5.22×10^{17}	20.86	1.73	0.58
SnSe/ZnO 10 cycles	1.78×10^{17}	12.33	0.35	2.84
SnSe/ZnO 40 cycles	3.93×10^{17}	6.29	0.40	2.53
SnSe/ZnO 100 cycles	2.82×10^{15}	3.82	1.54×10^{-3}	649.35
SnSe[28]	2.93×10^{17}	49.37	2.31	
SnSe[29]	3.0×10^{17}	13.82	0.8	
SnSe[30]	1.3×10^{17}	42.1	0.88	

[a]Reported data in the literature for polycrystalline SnSe are included for comparison.

suggested that a nanostructured SnSe/SnS heterojunction can provide a higher Seebeck coefficient by scattering low-energy electrons (*i.e.*, energy filtering effect), thus producing a larger power factor.[12] Furthermore, decoupling three key thermoelectric parameters, such as the Seebeck coefficient, electrical conductivity, and thermal conductivity, is reportedly possible from the grain boundary engineering by atomic layer deposition (ALD).[13] For example, He *et al.* reported an improved thermoelectric performance for Al_2O_3-coated bismuth.[14] Moreover, Lee *et al.* demonstrated a near-single crystal thermoelectric property for polycrystalline SnSe by surface oxide removal *via* a chemical reduction process performed at 613 K in a 4% H_2/Ar atmosphere.[15] ALD-grown thin films have been known to effectively passivate the surface defects.[16,17] Therefore, ALD-based grain boundary engineering can enhance the electrical conductivity by increasing the effective carrier concentration. Additionally, the incorporation of ALD-grown ZnO into the $Bi_{0.4}Sb_{1.6}Te_3$ (BST) matrix has been demonstrated to effectively block the phonon propagation and tune the carrier density at the ZnO/BST heterogeneous grain boundaries.[18] The increase in electron mobility in Bi_2Te_3 powders after ZnO coating is associated with the defect passivation in the grain boundary.[19] Li *et al.* reported that the increase in electrical conductivity in $Bi_2Te_{2.7}Se_{0.3}$ powders after ZnO coating is due to the Te precipitation in the grain boundary.[20] To improve the device performance further, the temperature-dependent carrier transport properties of metal/SnSe contacts should be thoroughly understood. Previous research has focused on the electrical characterization of metal contacts to single-crystal SnSe.[21−25] However, research and information on the transport properties of metal contacts to polycrystalline SnSe is limited.[26,27] We prepared the ZnO-nanocoated polycrystalline SnSe with different ALD ZnO cycles and subsequently investigated their electrical properties in terms of carrier transport.

EXPERIMENTAL DETAILS

Materials Synthesis. First, we prepared SnSe powders by mechanical alloying using a planetary mill (Retch GmbH, PM400) at a rotation speed of 250 rpm for 50 h. An atomic ratio of 1:1 for Sn (RND Korea, 99.9%, 400 mesh) and Se (Alfa Aesar, 99.9%, 200 mesh) powders was used. After loading SnSe powders into a thermal ALD reactor (Atomic Shell, CN-1), ZnO thin films were deposited on the SnSe powders at 100 °C with pulse cycles of 10, 40, and 100. The ALD reactor was rotated at 30 rpm to avoid the agglomeration of the SnSe powders. Diethylzinc [DEZn: $Zn(C_2H_5)_2$] and H_2O were supplied as the Zn and oxygen precursors, respectively, and the ALD pulse was supplied as a sequence of DEZn feeding for 0.5 s, N_2 purge for 15 s, H_2O feeding for 0.5 s, and N_2 purge for 15 s. Analysis of the data obtained from transmission electron microscopy equipped with energy-dispersive X-ray spectroscopy (TEM−EDS; JEM-2100F, JEOL) revealed that the thicknesses of the coated ZnO layers were approximately 6, 15, and 19 nm for 10, 40, and 100 cycles, respectively. Subsequently, the ZnO-coated SnSe powders were sintered by spark plasma sintering (SPS; SPS-825, SPS Syntex Inc.) at 773 K for 5 min at a compressive pressure of 60 MPa and a heating rate of 50 K/min, which produced ZnO-coated SnSe pellets.

Device Fabrication and Characterization. To explore their electrical properties, 50 nm thick Pt Schottky contacts with circular shapes (diameter: 500 μm) and large-area 100 nm thick Al back contacts were deposited using radio-frequency magnetron sputtering. Before depositing the metal layers, chemical treatment was performed using a HCl/H_2O (1:1) solution. A schematic of a Schottky diode is shown in Figure 1. Current−voltage (I−V) characteristics were tested using a Keithley 238 current source and a probe station with a thermal chuck at different temperatures in the range of 300−450 K. Note that the current values for both Pt/SnSe/Al and Pt/

https://doi.org/10.1021/acsomega.2c05584
ACS Omega 2022, 7, 41606−41613

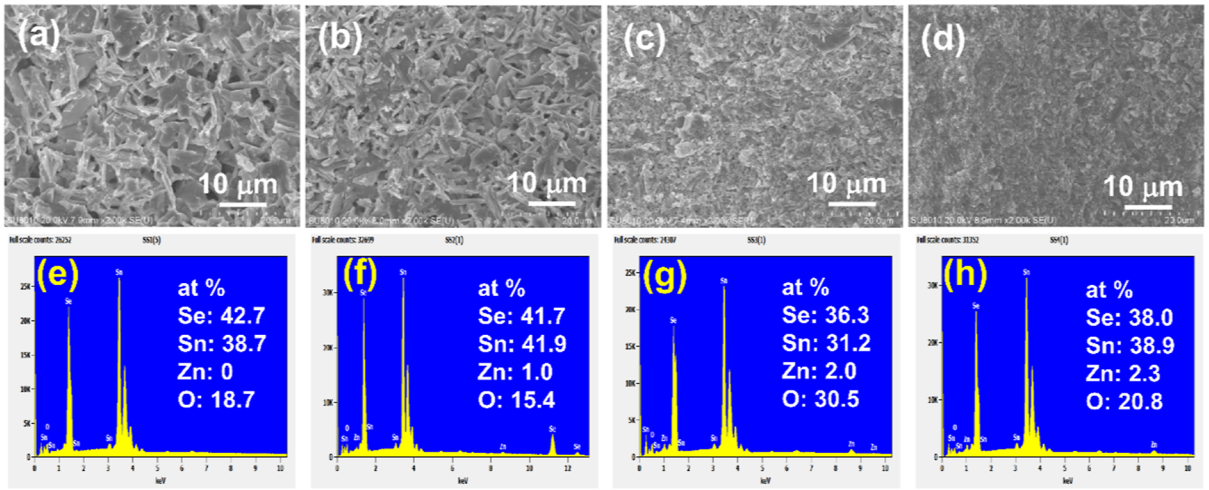

Figure 2. SEM images of SnSe pellets (a) without ZnO coating, (b) with ZnO 10 cycles, (c) with ZnO 40 cycles, and (d) with ZnO 100 cycles. EDS patterns of SnSe pellets (e) without ZnO coating, (f) with ZnO 10 cycles, (g) with ZnO 40 cycles, and (h) with ZnO 100 cycles.

SnSe/Pt contacts were similar, which indicates that the energy barriers for SnSe/Pt (high work function) and SnSe/Al (low work function) would be similar. Furthermore, we did not perform thermal annealing to avoid any variance owing to the reaction at the SnSe/Al interface.

RESULTS AND DISCUSSION

The electrical properties obtained from the Hall effect measurements at room temperature are listed in Table 1. The Hall coefficient values for the prepared samples were found to be positive, thus implying p-type conduction. Note that the electrical properties of the SnSe sample are comparable to those of previous studies.[28−30] Evidently, the electrical conductivity decreased slightly for the SnSe samples with ZnO 10 and 40 cycles. However, the carrier concentration decreased significantly for the SnSe sample with ZnO 100 cycles, thus indicating that the carriers in SnSe were compensated by the ZnO coating. Owing to this compensation effect, increased resistivity and decreased conductivity were observed. During the ALD process, Zn and oxygen atoms can diffuse into the SnSe layers. Zn doping in SnSe increases the p-type conductivity.[31] The hole concentration increases if Zn diffusion into SnSe is dominant. Meanwhile, oxygen diffusion can produce oxidized phases, such as SnO and SnO_2, thus exhibiting p- and n-type conductivity, respectively.[32] Because the hole concentration for the SnSe sample with ZnO 100 cycles reduced significantly, the SnO_2 phase might be formed predominantly near the ZnO/SnSe interface.

Reportedly, the interfacial layer detected in the HfO_2 (2 nm)/InP junction was not observed in the HfO_2 (>6 nm)/InP junction, which is associated with the self-cleaning effect.[33] An approximately 9 nm thick Al_2O_3 layer deposited by ALD on a 2.8 nm thick native oxide-covered InSb layer was found to effectively remove the native oxide by the self-cleaning effect.[34] An approximately 7 nm thick HfO_2 film deposited by ALD on native oxide-covered InGaAs was found to exhibit a similar effect.[35] A lower density of interface states was observed for the ZnO (10 nm)/InP junction as compared to the ZnO (5 nm)/InP junction.[36] We believe that the defective interfacial layer that remained in the SnSe sample with ZnO 10 cycles might reduce the hole concentration and conductivity. For the SnSe sample with 40 cycles, this defective layer might have been removed by the self-cleaning effect, which increased the hole concentration again, as presented in Table 1. However, the exact underlying mechanism requires further investigation.

The morphology of the ZnO-coated SnSe pellets was examined using scanning electron microscopy (SEM). Figure 2a−h shows SEM images and the corresponding EDS patterns measured on the SnSe samples with ZnO 0, 10, 40, and 100 cycles, respectively. As the number of ALD pulse cycles increased, the surface morphology smoothed. The elemental analysis of the EDS patterns suggests the presence of Zn and O atoms in the ZnO-coated samples.

Figure 3 shows the $I-V$ data at 300 K for each sample. A decrease in current values was observed with increasing ALD

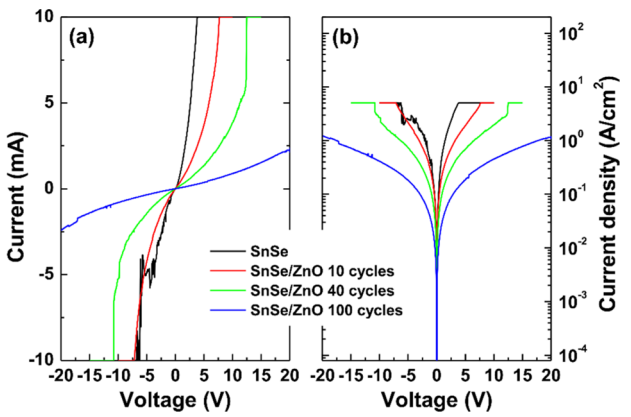

Figure 3. (a) Current−voltage ($I-V$) and (b) current density−voltage ($J-V$) curves measured at 300 K.

ZnO cycles. The carriers would have more difficulty traveling across the ZnO layer for thicker ZnO layers. Figure 4 shows the temperature-dependent current density−voltage ($J-V$) curves for each sample. All the samples exhibited an increase in current values with increasing temperature; this trend was the most significant for the SnSe sample with ZnO 100 cycles. The different temperature dependences for each sample also indicate that different carrier transport mechanisms were involved. The rectifying ratios at ±3 V were approximately 1 for all samples and at all temperatures.

https://doi.org/10.1021/acsomega.2c05584
ACS Omega 2022, 7, 41606−41613

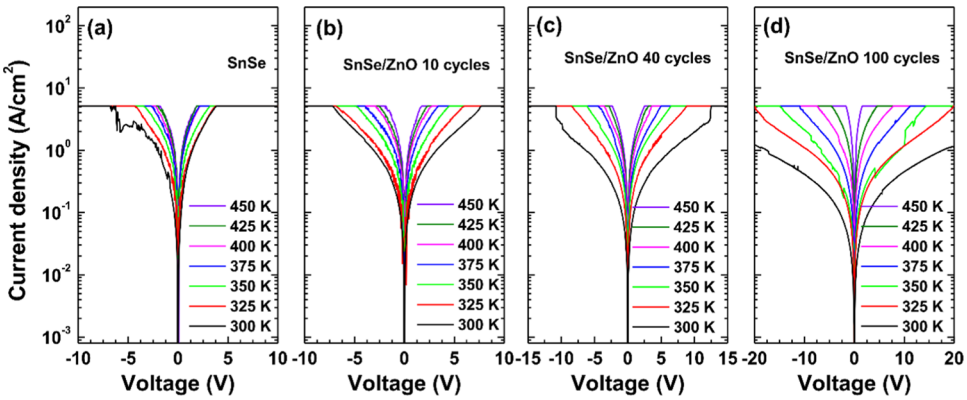

Figure 4. Temperature-dependent current density–voltage (J–V–T) curves for (a) SnSe, (b) SnSe with ZnO 10 cycles, (c) SnSe with ZnO 40 cycles, and (d) SnSe with ZnO 100 cycles.

The increase in current values with the temperature, shown in Figure 4, indicates that the thermal activation process with an $\exp(-E_A/kT)$ dependence, where E_A is the activation energy, contributed to the current conduction.[37] Figure 5a shows the plots of reverse current versus $1/kT$ at −1 V. From the linear fits to these plots, the E_A values corresponding to the effective energy barrier for current conduction could be obtained. Figure 5b shows the E_A values at different bias voltages, thus indicating the highest values for the SnSe sample with ZnO 100 cycles. The activation energy is an indicator for the presence of interfacial traps/defects related to trap-assisted recombination. With the exception of the ZnO layer, the prepared samples had the same configuration. Therefore, the higher activation energy with a thicker ZnO layer indicates that passivation of interfacial traps/defects by ZnO deposition occurred more effectively.

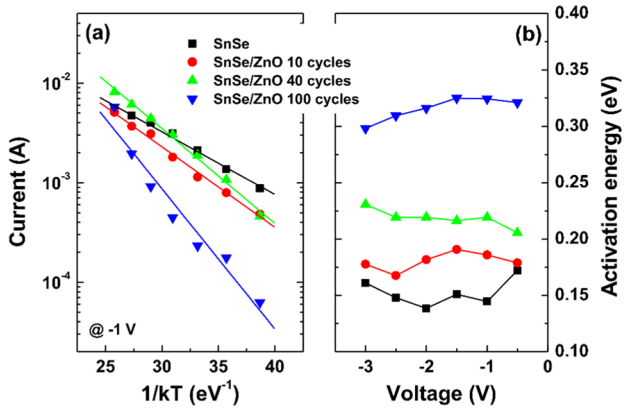

Figure 5. (a) Plots of reverse current *vs* $1/kT$ at −1 V and (b) activation energies at different voltages.

As shown in Figure 4, the linear regions of the semi-logarithmic J–V curves were significantly narrow. Hence, instead of using the conventional thermionic emission (TE) model, we employed the Cheung and Cheung method to calculate the electrical properties such as the ideality factor (n), barrier height (φ_B), and series resistance (R_S) using the following equations.[38]

$$\frac{dV}{d(\ln I)} = \frac{nkT}{q} + IR_S \quad (1)$$

$$H(I) = V - \frac{nkT}{q}\ln\left(\frac{I}{AA^*T^2}\right) \quad (2)$$

where $H(I) = n\varphi_B + IR_S$ and A^* is the effective Richardson constant (18 A/cm² K² for p-SnSe).[21]

Figure 6 shows plots of $dV/d(\ln I)$ and $H(I)$ *versus* I at 300 K, and the same method was applied to other temperatures.

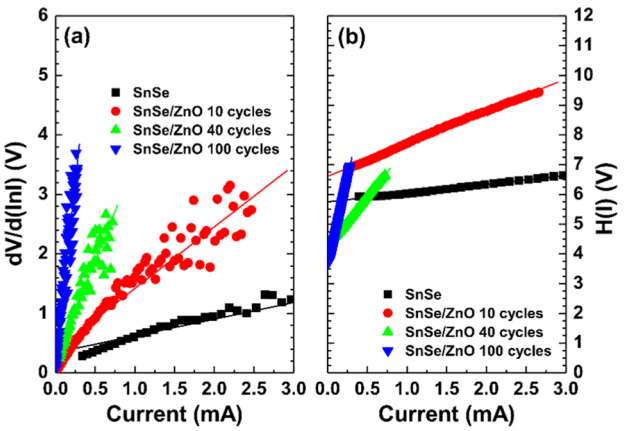

Figure 6. Plots of (a) $dV/d(\ln I)$ and (b) $H(I)$ *vs* current (I) measured at 300 K.

The calculated barrier heights and ideality factors are shown in Figure 7a,b, respectively, and reveal an increase in the barrier

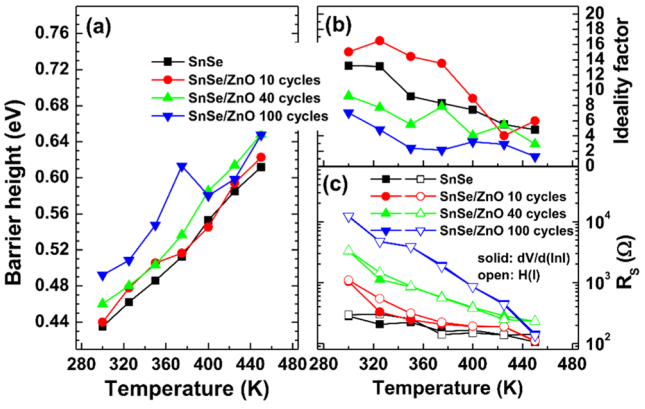

Figure 7. Temperature dependence of (a) barrier height, (b) ideality factor, and (c) series resistance obtained from forward bias I–V data.

https://doi.org/10.1021/acsomega.2c05584
ACS Omega 2022, 7, 41606−41613

height and a decrease in the ideality factor with temperature. This phenomenon is attributed to barrier inhomogeneity. The difference in the barrier height for each sample was insignificant, essentially exhibiting similar values. However, the difference in the ideality factor for each sample was distinct. Furthermore, the lowest ideality factor was observed for the SnSe sample with ZnO 100 cycles. A greater than unity ideality factor can result from image force lowering, tunneling, generation−recombination, the presence of low Schottky barrier patches, interface impurities/nonuniform interfaces, and interfacial layers.[39,40] Table 2 lists the Schottky diode parameters reported in the literature for metal/SnSe contacts.

Table 2. Summary of Reported Results in the Literature for Metal/SnSe Schottky Contacts[a]

Schottky contacts	SnSe types	barrier height (eV)	ideality factor	ref
Cu	thin film on glass	0.50	1.58	5
Ag	single crystal	∼0.5	∼3.5	21*
In	single crystal	0.318	3.665	22*
Ag	single crystal	0.495	6.17	23*
Ag	single crystal	0.512	3.27	24*
Al	single crystal	∼0.7	∼1.2	25*
In	thin film on Si	0.66	3.71	26
Ag	thin film on glass	∼0.77	∼1.7	27*
Pt	SnSe pellets without ZnO coating	0.44	13.2	present work*
Pt	SnSe pellets with ZnO 100 cycles	0.49	7.0	present work*

[a][*]indicates that $I-V-T$ measurements were performed.

As shown in Figure 7c, the series resistance at 300 K was the largest for the SnSe sample with ZnO 100 cycles. The thicker ZnO layer was the primary contributor to the high series resistance. The variation in the series resistance for each sample was in accordance with that of the resistivity presented in Table 1. In particular, the series resistance at 450 K was similar for each sample. Therefore, the effect of the thickness of the ZnO layer on the series resistance was negligible at this temperature. Electron injection from the Pt electrode to the Zn layer would increase with temperature; thus, the difference in series resistance of the ZnO layer became small.

Figure 8a shows the plots of the barrier height *versus* the ideality factor. Linearity between the two factors was observed,

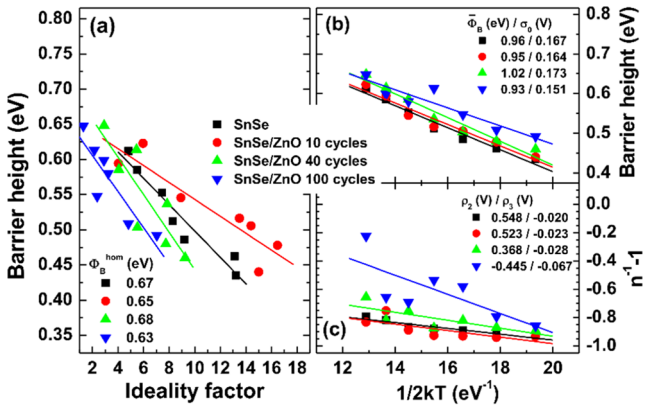

Figure 8. (a) Plots of barrier height *vs* ideality factor, (b) plots of barrier height *vs* $1/2kT$, and (c) plots of $(n^{-1} - 1)$ *vs* $1/2kT$.

thus indicating the presence of a lateral barrier inhomogeneity.[41] The linear extrapolation to $n = 1$ produced a homogeneous barrier height (φ_B^{hom}). Almost similar φ_B^{hom} values of 0.67, 0.65, 0.68, and 0.63 eV were obtained for the SnSe samples with ZnO 0, 10, 40, and 100 cycles, respectively. The Schottky barrier inhomogeneity over the contact area was characterized by assuming a Gaussian distribution, wherein ϕ_B and n are described as follows.[42]

$$\varphi_B = \overline{\varphi}_B - \frac{q\sigma_0^2}{2kT} \tag{3}$$

$$\frac{1}{n} - 1 = -\rho_2 + \frac{q\rho_3^2}{2kT} \tag{4}$$

where $\overline{\varphi}_B$ is the zero-bias mean barrier height, σ_0 is the standard deviation whose temperature dependence is negligibly small, and ρ_2 and ρ_3 are the temperature-independent voltage coefficients of the mean barrier height and the standard deviation, respectively. Based on eq 3, the plots of φ_B*versus* $1/2kT$ are shown in Figure 8b. The linear fits to the plots produced the values of $\overline{\varphi}_B$, which were highest for the SnSe sample with ZnO 40 cycles. The $\overline{\varphi}_B$ values were also higher than the effective barrier height. The value of σ_0 is the highest for the SnSe sample with ZnO 40 cycles and the lowest for the SnSe sample with ZnO 100 cycles. A lower value of σ_0 indicates that the barrier inhomogeneity was improved.

According to Dobrocka and Osvald,[43] the largest standard deviation is related to the strongest temperature dependence of the barrier height. Therefore, the zero-bias mean barrier height was the highest for the SnSe sample with ZnO 40 cycles. As shown in Figure 8c, the linear relationship between $(n^{-1} - 1)$ and $1/2kT$ assures the voltage dependence of the inhomogeneous barrier. The negative values of ρ_3 imply that the standard deviation (*i.e.*, the spatial fluctuation of the barrier height) decreases as the bias voltage increases, which is related to the image force lowering.[42] Thus, the highest ρ_3 value for the SnSe sample with ZnO 100 cycles indicates that the distribution of the barrier height became more homogeneous with the applied bias voltage. In addition, Chand and Kumar reported that with an increase in the standard deviation, the ideality factor increased significantly at low temperatures.[44] Therefore, the lowest ideality factor for the SnSe sample with ZnO 100 cycles would be related to the lowest standard deviation.

To obtain the reverse bias barrier height at each temperature, we used the following equation[45]

$$J = J_0 \exp\left(-\frac{qV}{nkT}\right)\left[1 - \exp\left(-\frac{qV}{kT}\right)\right] \tag{5}$$

$$J_0 = A^* T^2 \exp\left(-\frac{q\varphi_B}{kT}\right) \tag{6}$$

where J_0 is the reverse bias saturation current density. Herein, $\ln(J_0)$ can be extrapolated from the intercept of the logarithmic plots of $J/[1 - \exp(-qV/kT)]$ versus V. As an example, Figure 9a shows plots for the SnSe sample. The barrier heights obtained for each sample are shown in Figure 9b. Similar to the forward bias barrier height shown in Figure 7a, the barrier height increased with the temperature. The differences in each sample were insignificant. According to eq 3, the values of $\overline{\varphi}_B$ and σ_0 were obtained from the plots of φ_B*versus* $1/2kT$ shown in Figure 10a. Similarly, slightly lower $\overline{\varphi}_B$ values than those from the forward bias $I-V$ characteristics were observed. In

https://doi.org/10.1021/acsomega.2c05584
ACS Omega 2022, 7, 41606−41613

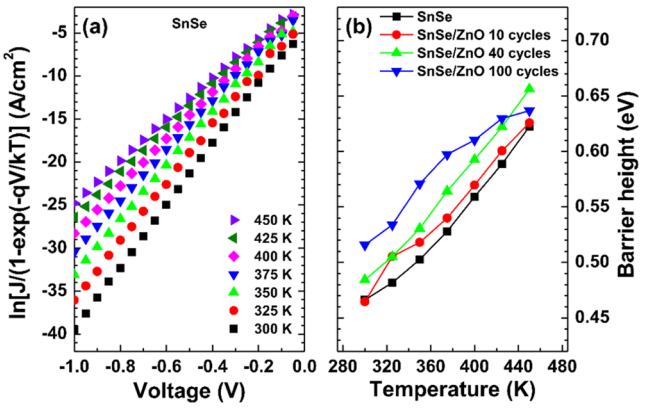

Figure 9. (a) Logarithmic plot of $J/[1 - \exp(-qV/kT)]$ *vs* V for the SnSe sample and (b) barrier height obtained from reverse bias $I-V$ data.

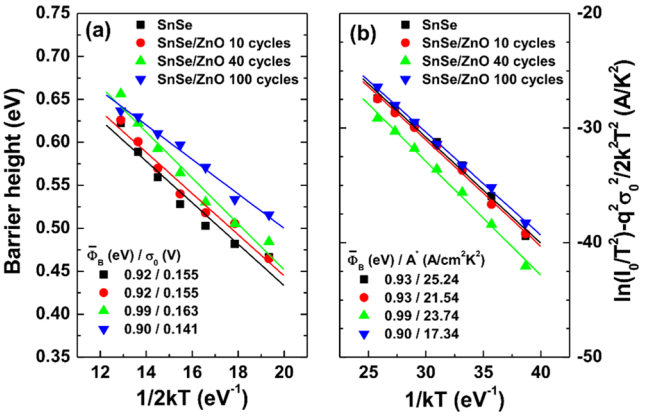

Figure 10. (a) Plots of barrier height *vs* $1/2kT$ and (b) modified Richardson plots.

addition, the highest (lowest) σ_0 was observed for the SnSe sample with ZnO 40 (100) cycles, which is the same for the forward bias current characteristics.

According to the barrier inhomogeneity model, the Richardson plot can be modified as follows[42]

$$\ln\left(\frac{I_0}{T^2}\right) - \frac{q^2\sigma_0^2}{2k^2T^2} = \ln(AA^*) - \frac{q\bar{\varphi}_B}{kT} \quad (7)$$

Figure 10b shows the plots of $\ln(I_0/T^2) - q^2\sigma_0^2/2k^2T^2$*versus* $1/kT$. The linear fitting yielded the zero-bias mean barrier heights of 0.93, 0.93, 0.99, and 0.90 eV for the SnSe samples with ZnO 0, 10, 40, and 100 cycles, respectively, which are very similar to the mean barrier heights from the φ_B*versus* $1/2kT$ plots shown in Figure 10a. The intercepts at the ordinate produced the effective Richardson constants of A^* of 25.24, 21.54, 23.74, and 17.34 A cm^{-2} K^{-2} for the SnSe samples with ZnO 0, 10, 40, and 100 cycles, respectively. These results are similar to the theoretical value of 18 A cm^{-2} K^{-2} for *p*-SnSe, thereby confirming that Schottky barrier inhomogeneity is involved in the carrier transport.

Based on the above analysis, a possible energy band diagram for the Pt/ZnO-coated SnSe junctions was drawn schematically, as shown in Figure 11a. The band gap (E_g) and electron affinity (χ) of ZnO were 3.37 and 4.35 eV, respectively,[46] whereas these values for SnSe were 1.25 and 4.7 eV, respectively.[47] Both the conduction band offset and the valence band offset were calculated using the method

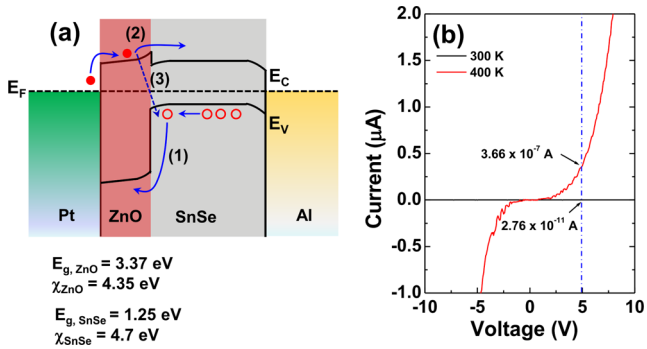

Figure 11. (a) Energy band diagram of ZnO-coated SnSe and (b) $I-V$ data for Pt contacts to 65 nm thick ZnO grown on a glass substrate at 96 °C.

suggested by Kraut *et al.*[48] The barrier height for Pt contact to the ZnO film was obtained as 0.8 eV. Hence, the barrier height of Pt/ZnO was assumed to be approximately 0.8 eV. As mentioned above, the energy barriers for SnSe/Pt and SnSe/Al are possibly similar. Hence, the barrier height of the SnSe/Al contact was assumed to be approximately 0.5 eV. From the Hall effect measurement, the carrier concentration of the 20 nm thick ZnO film grown on a glass substrate at 100 °C was found to be approximately 3×10^{14} cm^{-3}. Because of the low carrier concentration, the thin ZnO coating layer was completely depleted after the ZnO/SnSe junction was formed. Thus, electron injection from ZnO to SnSe did not occur effectively. Instead, hole injection from SnSe to ZnO (denoted as no. 1) was the main contributor to the current flow. For a higher number of ALD ZnO cycles, holes should travel across the thicker ZnO layer, which increased the series resistance.

As shown in Figure 11b, we found that in Pt contact to approximately 65 nm thick ZnO grown on a glass substrate at 96 °C, the current value increased with the increase in ambient temperature from 300 to 400 K. For example, it increased by approximately 4 orders of magnitude at 5 V. With increasing temperature, more electrons in the Pt electrode gained sufficient energy to surmount the energy barrier at the Pt/ZnO interface, thereby contributing to the current conduction. Similarly, the increased current in the Pt/ZnO-coated SnSe junction at high temperatures could be explained by electron injection from the Pt electrode to ZnO (denoted as no. 2). In addition, the hole injection from SnSe also increased, thereby contributing to the current conduction. Electrons in ZnO could conform to holes in SnSe *via* the interface states (denoted as no. 3), which is detrimental to current flow. This indicates that process 3 is strong when numerous interface states are present at the ZnO/SnSe interface. Therefore, the increased current values at high temperatures also indicate that the interface states were effectively passivated at the ZnO/SnSe interface.

From the perspective of thermoelectric devices, a high electrical conductivity must be maintained. Therefore, note that the conductivity of the SnSe samples with ZnO 10 and 40 cycles decreased slightly compared with the sample without ZnO coating. The ZnO-coated SnSe samples in this study were used as thermoelectric devices operating in the mid-temperature range (400–900 K). Although the diode properties were quite poor, the results revealed similar electrical parameters, such as barrier height and series resistance, particularly at 450 K. Therefore, ZnO nanocoating can provide improved interfacial properties without degrading the electrical con-

https://doi.org/10.1021/acsomega.2c05584
ACS Omega 2022, 7, 41606−41613

ductivity. Consequently, our results indicate that ZnO-coated SnSe can be considered for future thermoelectric device applications.

CONCLUSIONS

We prepared ZnO-coated SnSe powders by ALD with different numbers of ZnO pulse cycles and investigated the current conduction mechanisms of the Pt/ZnO-coated SnSe junctions. At 300 K, lower current and higher series resistance were observed with an increasing number of ZnO pulse cycles (*i.e.*, ZnO thickness). However, the current and series resistances were similar at 450 K. The difference in the barrier height for each sample was trivial, thus suggesting that the ZnO coating did not alter barrier formation at the Pt/SnSe junction. Schottky barrier inhomogeneity was involved in forward and reverse bias current conduction. The lowest standard deviation for SnSe with ZnO 100 cycles indicated a lower spatial fluctuation for barrier heights, which is related to the lowest ideality factor. The results obtained from the present work demonstrate that the diode performance is similar to that of the ZnO coating, thus suggesting that ZnO-coated SnSe by ALD is a good alternative for thermoelectric devices.

AUTHOR INFORMATION

Corresponding Authors

Hogyoung Kim − *Department of Visual Optics, Seoul National University of Science and Technology (Seoultech), Seoul 01811, Republic of Korea;* orcid.org/0000-0003-0066-2584; Email: hogyoungkim@gmail.com

Byung Joon Choi − *Department of Materials Science and Engineering, Seoul National University of Science and Technology (Seoultech), Seoul 01811, Republic of Korea;* Email: bjchoi@seoultech.ac.kr

Authors

Myeong Jun Jung − *Department of Visual Optics, Seoul National University of Science and Technology (Seoultech), Seoul 01811, Republic of Korea*

Jongmin Byun − *Department of Visual Optics, Seoul National University of Science and Technology (Seoultech), Seoul 01811, Republic of Korea*

Min Hwan Lee − *Department of Mechanical Engineering, University of California Merced, Merced, California 95343, United States;* orcid.org/0000-0002-3490-6607

Complete contact information is available at: https://pubs.acs.org/10.1021/acsomega.2c05584

Notes

The authors declare no competing financial interest.

ACKNOWLEDGMENTS

This work was supported by the National Research Foundation of Korea (NRF) grant funded by the Korea government (MSIT) (2022R1A4A5033917).

REFERENCES

(1) Chen, Z.; Shi, X.; Zhao, L.; Zou, J. High-performance SnSe thermoelectric materials: Progress and future challenge. *Prog. Mater. Sci.* **2018**, *97*, 283−346.

(2) Reddy, V. R. M.; Gedi, S.; Pejjai, B.; Park, C. Perspectives on SnSe-based thin film solar cells: a comprehensive review. *J. Mater. Sci.: Mater. Electron.* **2016**, *27*, 5491−5508.

(3) Su, Y.; Ebrish, M.; Olson, E.; Koester, S. $SnSe_2$ field-effect transistors with high drive current. *Appl. Phys. Lett.* **2013**, *103*, 263104.

(4) Davitt, F.; Manning, H.; Robinson, F.; Hawken, S.; Biswas, S.; Petkov, N.; Druenen, M.; Boland, J.; Reid, G.; Holmes, J. Crystallographically controlled synthesis of SnSe nanowires: potential in resistive memory devices. *Adv. Mater. Interfaces* **2020**, *7*, 2000474.

(5) Jagani, H.; Gupta, S.; Bhoraniya, K.; Navapariya, M.; Pathak, V.; Solanki, G.; Patel, H. Photosensitive Schottky barrier diodes based on Cu/p-SnSe thin films fabricated by thermal evaporation. *Adv. Mater.* **2022**, *3*, 2425.

(6) Patel, K.; Solanki, G.; Patel, K.; Pathak, V.; Chauhan, P. Investigation of optical, electrical and optoelectronic properties of SnSe crystals. *Eur. Phys. J. B* **2019**, *92*, 1−11.

(7) Duvjir, G.; Min, T.; Thi Ly, T.; Kim, T.; Duong, A.; Cho, S.; Rhim, S.; Lee, J.; Kim, J. Origin of p-type characteristics in a SnSe single crystal. *Appl. Phys. Lett.* **2017**, *110*, 262106.

(8) Zhao, L.; Lo, S.; Zhang, Y.; Sun, H.; Tan, G.; Uher, C.; Wolverton, C.; Dravid, V.; Kanatzidis, M. Ultralow thermal conductivity and high thermoelectric figure of merit in SnSe crystals. *Nature* **2014**, *508*, 373−377.

(9) Zhao, L.; Chang, C.; Tan, G.; Kanatzidis, M. SnSe: a remarkable new thermoelectric material. *Energy Environ. Sci.* **2016**, *9*, 3044−3060.

(10) Liu, S.; Sun, N.; Liu, M.; Sucharitakul, S.; Gao, X. Nanostructured SnSe: synthesis, doping, and thermoelectric properties. *J. Appl. Phys.* **2018**, *123*, 115109.

(11) Heo, S.; Jo, S.; Kim, H.; Choi, G.; Song, J.; Kang, J.; Park, N.; Ban, H.; Kim, F.; Jeong, H.; Jung, J.; Jang, J.; Lee, W.; Shin, H.; Son, J. Composition change-driven texturing and doping in solution-processed SnSe thermoelectric thin films. *Nat. Commun.* **2019**, *10*, 864.

(12) Zhang, R.; Zhou, Z.; Yao, Q.; Qi, N.; Chen, Z. Significant improvement in thermoelectric performance of SnSe/SnS via nanoheterostructures. *Phys. Chem. Chem. Phys.* **2021**, *23*, 3794.

(13) Li, S.-K.; Zhu, W.-M.; Xiao, Y.-G.; Pan, F. Improving the performance of thermoelectric materials by atomic layer deposition-based grain boundary engineering. *Chin. J. Struct. Chem.* **2020**, *39*, 831−837.

(14) He, S.; Bahrami, A.; Zhang, X.; Martínez, I.; Lehmann, S.; Nielsch, K. Effect of powder ALD interface modification on the thermoelectric performance of bismuth. *Adv. Mater. Technol.* **2022**, *7*, 2100953.

(15) Lee, Y.; Luo, Z.; Cho, S.; Kanatzidis, M. I.; Chung, I. Surface oxide removal for polycrystalline SnSe reveals near-single-crystal thermoelectric performance. *Joule* **2019**, *3*, 719−731.

(16) Repo, P.; Talvitie, H.; Li, S.; Skarp, J.; Savin, H. Silicon surface passivation by Al_2O_3: effect of ALD reactants. *Energy Proc.* **2011**, *8*, 681−687.

(17) Zhou, L.; Bo, B.; Yan, X.; Wang, C.; Chi, Y.; Yang, X. Brief review of surface passivation on III-V semiconductor. *Crystals* **2018**, *8*, 226.

(18) Kim, K.; Lim, S.; Lee, S.; Hong, J.; Cho, D.; Mohamed, A.; Koo, C.; Baek, S.; Kim, J.; Kim, S. Precision interface engineering of an atomic layer in bulk Bi_2Te_3 alloys for high thermoelectric performance. *ACS Nano* **2019**, *13*, 7146−7154.

(19) Jung, M. J.; Ji, M.; Han, J. H.; Lee, Y.-I.; Oh, S.-T.; Lee, M. H.; Choi, B. J. Atomic layer deposition of ZnO layers on Bi_2Te_3 powders: Comparison of gas fluidization and rotary reactors. *Ceram. Int.* **2022**, DOI: 10.1016/j.ceramint.2022.08.241. (in press)

(20) Li, S.; Liu, Y.; Liu, F.; He, D.; He, J.; Luo, J.; Xiao, Y.; Pan, F. Effective atomic interface engineering in $Bi_2Te_{2.7}Se_{0.3}$ thermoelectric material by atomic-layer-deposition approach. *Nano Energy* **2018**, *49*, 257−266.

(21) Tuğluoğlu, N.; Karadeniz, S.; Sahin, M.; Safak, H. Temperature-dependent barrier characteristics of Ag/p-SnSe Schottky diodes based on I−V−T measurements. *Semicond. Sci. Technol.* **2004**, *19*, 1092−1097.

(22) Patel, H.; Patel, K.; Patel, A.; Jagani, H.; Patel, K.; Solanki, G.; Pathak, V. Temperature-dependent I−V characteristics of In/p-SnSe Schottky diode. *J. Electron. Mater.* **2021**, *50*, 5217−5225.
(23) Şafak, H.; Şahin, M.; Yüksel, Ö. F. Analysis of I−V measurements on Ag/p-SnS and Ag/p-SnSe Schottky barriers. *Solid State Electron.* **2002**, *46*, 49−52.
(24) Karadeniz, S.; Tuğluoğlu, N.; Şahin, M.; Şafak, H. Series resistance calculation for Ag contacts on single crystal layered p-SnS and p-SnSe compound semiconductors in the wide temperature range. *Microelectron. Eng.* **2005**, *81*, 125−131.
(25) Sumesh, C.; Patel, K.; Menbari, E. Analysis of barrier height inhomogeneities in Al-pSnSe Schottky diode. *Eur. Phys. J. Appl. Phys.* **2012**, *59*, 10103.
(26) Coskun, E.; Gullu, H.; Emir, C.; Parlak, M. Improvement of electrical characteristics of SnSe/Si heterostructure by integration of Si nanowires. *Physica B* **2021**, *604*, 412669.
(27) Patel, K. K.; Patel, K. D.; Patel, M.; Hingarajiya, K.; Pathak, V. Investigations on tin selenide thin film based Schottky barrier diodes by I-V-T method. *Adv. Mater. Res.* **2013**, *665*, 297−301.
(28) Fu, Y.; Xu, J.; Liu, G.; Tan, X.; Liu, Z.; Wang, X.; Shao, H.; Jiang, H.; Liang, B.; Jiang, J. Study on thermoelectric properties of polycrystalline SnSe by Ge doping. *J. Electron. Mater.* **2017**, *46*, 3182−3186.
(29) Li, C.; Wu, H.; Zhang, B.; Zhu, H.; Fan, Y.; Lu, X.; Sun, X.; Zhang, X.; Wang, G.; Zhou, X. High thermoelectric performance of co-doped p-type polycrystalline SnSe via optimizing electrical transport properties. *ACS Appl. Mater. Interfaces* **2020**, *12*, 8446−8455.
(30) Cai, B.; Li, J.; Sun, H.; Zhao, P.; Yu, F.; Zhang, L.; Yu, D.; Tian, Y.; Xu, B. Sodium doped polycrystalline SnSe: High pressure synthesis and thermoelectric properties. *J. Alloys Compd.* **2017**, *727*, 1014−1019.
(31) Jamali-Sheini, F.; Cheraghizade, M.; Yousefi, R. Electrochemically synthesis and optoelectronic properties of Pb- and Zn-doped nanostructured SnSe films. *Appl. Surf. Sci.* **2018**, *443*, 345−353.
(32) Pan, X.; Fu, L. Oxidation and phase transitions of epitaxial tin oxide thin films on (1012) sapphire. *J. Appl. Phys.* **2001**, *89*, 6048−6055.
(33) Kang, Y.; Kim, C.; Cho, M.; Chung, K.; An, C.; Kim, H.; Lee, H.; Kim, C.; Lee, T. Thickness dependence on crystalline structure and interfacial reactions in HfO_2 films on InP (001) grown by atomic layer deposition. *Appl. Phys. Lett.* **2010**, *97*, 172108.
(34) Hou, C.; Chen, M.; Chang, C.; Wu, T.; Chiang, C. Interfacial cleaning effects in passivating InSb with Al_2O_3 by atomic layer deposition. *Electrochem. Solid-State Lett.* **2008**, *11*, D60.
(35) Chang, C.; Chiou, Y.; Chang, Y.; Lee, K.; Lin, T.; Wu, T.; Hong, M.; Kwo, J. Interfacial self-cleaning in atomic layer deposition of HfO_2 gate dielectric on $In_{0.15}Ga_{0.85}As$. *Appl. Phys. Lett.* **2006**, *89*, 242911.
(36) Kim, H.; Jung, M.; Choi, B. Barrier reduction and current transport mechanism in Pt/n-InP Schottky diodes using atomic layer deposited ZnO interlayer. *J. Mater. Sci.: Mater. Electron.* **2021**, *32*, 22792−22802.
(37) Li, Y.; Ng, G.; Arulkumaran, S.; Ye, G.; Liu, Z.; Ranjan, K.; Ang, K. Investigation of gate leakage current mechanism in AlGaN/GaN high-electron-mobility transistors with sputtered TiN. *J. Appl. Phys.* **2017**, *121*, 044504.
(38) Cheung, S.; Cheung, N. Extraction of Schottky diode parameters from forward current-voltage characteristics. *Appl. Phys. Lett.* **1986**, *49*, 85−87.
(39) Chand, S.; Kumar, J. Current−voltage characteristics and barrier parameters of Pd2Si/p-Si (111) Schottky diodes in a wide temperature range. *Semicond. Sci. Technol.* **1995**, *10*, 1680−1688.
(40) Tung, R. Electron transport at metal−semiconductor interfaces: general theory. *Phys. Rev. B: Condens. Matter Mater. Phys.* **1992**, *45*, 13509−13523.
(41) Mönch, W. Barrier heights of real Schottky contacts explained by metal-induced gap states and lateral inhomogeneities. *J. Vac. Sci. Technol., B* **1999**, *17*, 1867−1876.
(42) Werner, J.; Güttler, H. Barrier inhomogeneities at Schottky contacts. *J. Appl. Phys.* **1991**, *69*, 1522−1533.
(43) Dobročka, E.; Osvald, J. Influence of barrier height distribution on the parameters of Schottky diodes. *Appl. Phys. Lett.* **1994**, *65*, 575−577.
(44) Chand, S.; Kumar, J. Effects of barrier height distribution on the behavior of a Schottky diode. *J. Appl. Phys.* **1997**, *82*, 5005−5010.
(45) Çınar, K.; Yıldırım, N.; Coşkun, C.; Turut, A. Temperature dependence of current-voltage characteristics in highly doped Ag/p-GaN/In Schottky diodes. *J. Appl. Phys.* **2009**, *106*, 073717.
(46) Hwang, D.; Kang, S.; Lim, J.; Yang, E.; Oh, J.; Yang, J.; Park, S. p-ZnO/n-GaN heterostructure ZnO light-emitting diodes. *Appl. Phys. Lett.* **2005**, *86*, 222101.
(47) Reddy, V. R. M.; Gedi, S.; Pejjai, B.; Park, C. Perspectives on SnSe-based thin film solar cells: a comprehensive review. *J. Mater. Sci.: Mater. Electron.* **2016**, *27*, 5491−5508.
(48) Kraut, E.; Grant, R.; Waldrop, J.; Kowalczyk, S. Precise determination of the valence-band edge in X-ray photoemission spectra: application to measurement of semiconductor interface potential. *Phys. Rev. Lett.* **1980**, *44*, 1620−1623.

https://doi.org/10.1021/acsomega.2c05584
ACS Omega 2022, 7, 41606−41613